HIPPOCAMPUS 22:772–789 (2012)

Phase Precession and Variable Spatial Scaling in a Periodic Attractor Map Model of Medial Entorhinal Grid Cells With Realistic After-Spike Dynamics

Zaneta Navratilova,[1,2] Lisa M. Giocomo,[3,4] Jean-Marc Fellous,[2,5,6] Michael E Hasselmo,[3] and Bruce L. McNaughton[1,2,5*]

ABSTRACT: We present a model that describes the generation of the spatial (grid fields) and temporal (phase precession) properties of medial entorhinal cortical (MEC) neurons by combining network and intrinsic cellular properties. The model incorporates network architecture derived from earlier attractor map models, and is implemented in 1D for simplicity. Periodic driving of conjunctive (position × head-direction) layer-III MEC cells at theta frequency with intensity proportional to the rat's speed, moves an 'activity bump' forward in network space at a corresponding speed. The addition of prolonged excitatory currents and simple after-spike dynamics resembling those observed in MEC stellate cells (for which new data are presented) accounts for both phase precession and the change in scale of grid fields along the dorso-ventral axis of MEC. Phase precession in the model depends on both synaptic connectivity and intrinsic currents, each of which drive neural spiking either during entry into, or during exit out of a grid field. Thus, the model predicts that the slope of phase precession changes between entry into and exit out of the field. The model also exhibits independent variation in grid spatial period and grid field size, which suggests possible experimental tests of the model. © 2011 Wiley Periodicals, Inc.

KEY WORDS: path integration; dead reckoning; continuous attractor neural network; place cells; entorhinal stellate cells

INTRODUCTION

It is widely recognized that a major determinant of the spatial firing characteristics of hippocampal neurons (O'Keefe and Dostrovsky, 1971) is the integration of self-motion information (O'Keefe, 1976; O'Keefe and Nadel, 1978; McNaughton et al., 1996). A major class of neural models that have been proposed to account for integration of inputs uses "continuous attractor" neural networks (CANN) (Amari, 1977; Ben-Yishai et al., 1995; Skaggs et al., 1995; Zhang, 1996; Samsonovich and McNaughton, 1997; Compte et al., 2000). Continuous attractor networks, unlike discrete (point) attractors, have a continuum of states which are quasi-stable in the absence of external input. Inputs to the network can cause movement along the attractor manifold, thus integrating input such as angular movement of the head (Skaggs et al., 1995; Zhang, 1996) or distance traveled (Samsonovich and McNaughton, 1997; Doboli et al., 2000; Conklin and Eliasmith, 2005). The hippocampal network receives inputs that could support path integration: from "head-direction" cells that encode relative azimuth (Taube et al., 1990; Taube, 1995; Mizumori and Williams, 1993; Chen et al., 1994); and from a speed encoding system, that combines vestibular, optic flow, proprioception, and motor efference copy into a coherent signal (Terrazas et al., 2005).

Samsonovich and McNaughton (1997) proposed a model of how head direction and movement speed signals can be combined in a continuous attractor network to keep track of location, and suggested that the necessary circuitry and cell types might be found in CA3 or in the entorhinal cortex (EC). This model is essentially a 2D extension of continuous attractor models suggested by Skaggs et al. (1995) and Zhang (1996) to account for how head direction (HD) cells integrate head angular velocity to track relative head direction. In these CANNs, neurons representing a given parameter value (e.g., location or head direction) are connected to others representing nearby values. Thus, neurons encoding similar values support each other's activity. With global recurrent inhibition that limits total network activity, spontaneous activity, and some noise, a "bump" of activity centered on any of an approximately continuous set of parameters or neural states is the statistically most probable configuration. This bump may form spontaneously or may be created by transient external inputs. In Samsonovich and McNaughton (1997), the attractor network of place cells was coupled to an intermediate layer of neurons whose firing was conjunctive for position on

[1] **Department of Neuroscience, Canadian Centre for Behavioural Neuroscience, University of Lethbridge, Alberta, Canada;** [2] **GIDP Neuroscience, University of Arizona, Tucson, Arizona;** [3] **Department of Psychology and Program in Neuroscience, Center for Memory and Brain, Boston University, Boston, Massachusetts;** [4] **Department of Neuroscience, Kavli Institute for Systems Neuroscience and Centre for the Biology of Memory, MTFS, Norwegian University of Science and Technology, Trondheim, Norway;** [5] **Department of Psychology, University of Arizona, Tucson, Arizona;** [6] **Department of Applied Mathematics, University of Arizona, Tucson, Arizona**

Grant sponsor: US PHS; Grant number: NS 20331; Grant sponsor: Alberta Heritage Foundation for Medical Research Polaris Award

*Correspondence to: Bruce L. McNaughton Ph.D., Canadian Centre for Behavioural Neuroscience (Room EP1242), The University of Lethbridge, 4401 University Dr W, Lethbridge, AB, T1K 3M4, Canada. E-mail: bruce.mcnaughton@uleth.ca

Accepted for publication 19 January 2010
DOI 10.1002/hipo.20939
Published online 11 April 2011 in Wiley Online Library (wileyonlinelibrary.com).

the 2D manifold or "chart" (also referred to as a "map") and head direction, and modulated by linear velocity. The return connections from the conjunctive layer to the place cell layer were offset in a direction consistent with the corresponding HD component (see Fig. 1A for a 1D diagram of this connectivity). Thus, the intermediate, conjunctive cell layer moved the position of the activity bump in the chart, and translated the rat's movement in the environment into a movement through a 2D continuum of attractors or neural states. Each of these states could theoretically become associated with external landmark information, thus linking them to specific environmental locations. A problem that such a model encounters is that the number of neurons available to represent points in the plane cannot be limitless, so eventually the bump will encounter an edge. To avoid edge-effects, Samsonovich and McNaughton (1997) as well as Conklin and Eliasmith (2005) assumed there must be periodic boundary conditions in the network, making it equivalent to a torus. The implicit prediction of this "toroidal attractor map" hypothesis was that firing of cells on the attractor map would repeat at regular spatial intervals in a rectangular lattice.

Neurons with regularly repeating place fields were subsequently discovered in layer II of the medial EC (MEC) (Fyhn et al., 2004), and have since been named "grid cells" (Hafting et al., 2005). In the Samsonovich and McNaugthon (1997) model, place fields repeated in a rectangular grid, while the

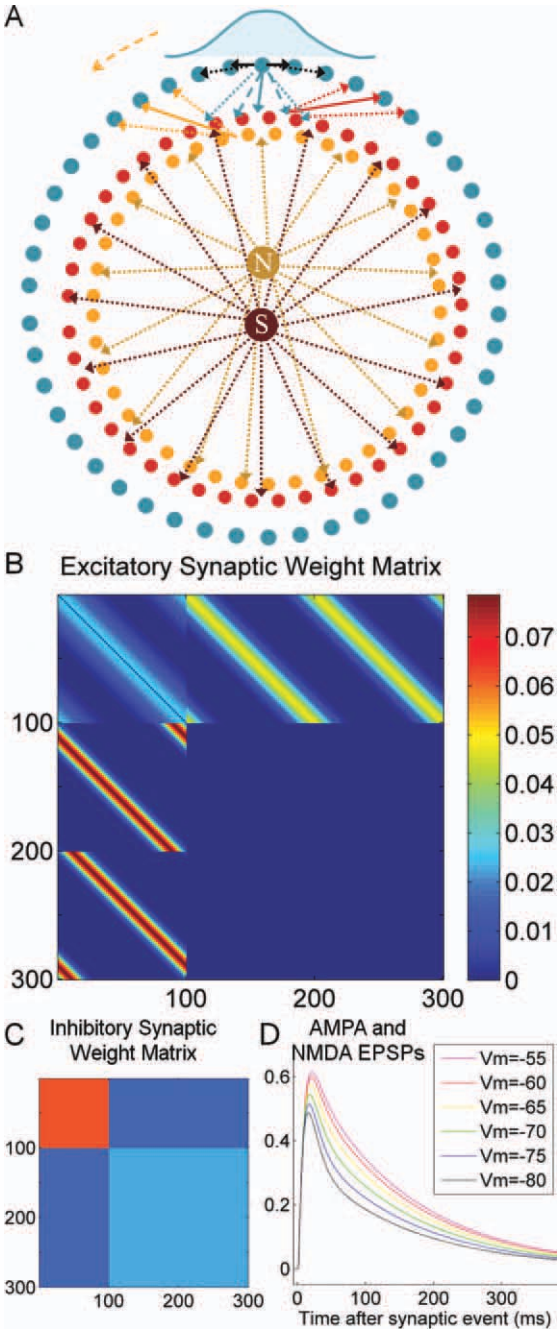

FIGURE 1. Toroidal attractor model and implementation of synaptic connections in simulations. A: One-dimensional representation of the network connectivity according to the toroidal attractor model. Grid cells (in blue) are arranged in a ring. Each grid cell has synaptic connections onto nearby neurons, with the synaptic strength decreasing as a Gaussian function of distance between neurons. Thus, a 'bump' of activity forms at one position. Grid cells project to conjunctive (grid-by-HD) cells (red and orange). Conjunctive cells also receive inputs from head-direction cells (light and dark brown), so that when the animal is moving north, the orange conjunctive cells are active. Conjunctive cells project back to the grid cell layer, with an offset in the relative direction which they represent. Thus, when the animal is moving north, the orange conjunctive cells activate the grid cells in the counterclockwise direction from the position of the grid cell activity bump and thus move the bump in the counterclockwise direction. B: Model grid and conjunctive network connection matrix. The strength of excitatory connections from all neurons (*y*-axis), to all neurons (*x*-axis) are displayed. The first 100 neurons are grid cells, and the upper left block shows their recurrent connections. Neurons 101–200 are "north" conjunctive cells, and the upper middle block shows their inputs from grid cells, while the left middle block shows their offset connections back to grid cells. Neurons 201–300 are "south" conjunctive cells. Note the symmetry of the grid cell to grid cell and grid cell to conjunctive cell connections and the asymmetry of the conjunctive cell to grid cell connections. C: Inhibitory neurons are not explicitly modeled, but global feed-back and feed-forward inhibition are implemented as inhibitory connections from all excitatory cells to all excitatory cells. Axes and scale are same as in excitatory weight matrix. Feedback inhibition within the grid cell layer is the strongest and feed-forward connections from grid to conjunctive, and from conjunctive to grid cells are weakest. Color scale is the same as in B. D: The result of AMPA and NMDA conductances in model grid cells starting at different membrane potentials. The AMPA component of the synaptic event is modeled as a single exponential, with a decay time constant of 10 ms. The NMDA component is a difference of exponentials, with a rise time constant of 2 µs, and a fall time constant of 150 ms. Displayed is the membrane potential resulting from a single excitatory synaptic event in a grid cell. The maximal conductance of the NMDA component is a fixed ratio of the AMPA component for all grid cell to grid cell synapses, but also depends on the membrane potential of the cell based on the relationship determined by Jahr and Stevens (1990; see Methods). Synapses from or to conjunctive cells only have an AMPA component and are not shown. [Color figure can be viewed in the online issue, which is available at wileyonlinelibrary.com.]

mathematically simplest unit describing a grid cell's firing grid is a rhombus (also referred to as a "triangular" grid). McNaughton et al. (2006) pointed out, however, that distorting a square map to a rhombus with periodic boundaries would result in rhomboidal grids of repeating place fields. This is equivalent to twisting a torus with a square unit cell, as was recently implemented analytically by Guanella et al. (2007). In addition to grid cells, Sargolini et al. (2006) have identified other cell types, deeper in MEC, corresponding to the two other essential ingredients of the Samsonovich and McNaughton (1997) model: pure HD cells, and grid location-by-HD ("conjunctive") cells, all exhibiting firing rate increases with running speed as predicted by the model. Thus, all of the components of Samsonovich and McNaughton's model for path integration appear to be present in the MEC. In further support for path integration via a continuous attractor occurring in the MEC, each pair of grid cells recorded at the same dorso-ventral location in the MEC has grid fields the same distance apart and with the same orientation relative to each other in all environments (Fyhn et al., 2007). This supports the idea that a single continuous attractor manifold could exist in a module of connected MEC neurons. Hippocampal neurons, in contrast, show random remapping of their relative field locations in different environments, and thus multiple attractor manifolds ("charts") would have to exist there to support path integration as well as this remapping (Samsonovich and McNaughton, 1997).

As was first observed in place cells of the hippocampus proper (Jung et al., 1994; Maurer et al., 2005), the size of grid fields (and the spacing between fields) increases in cells recorded more ventrally in the MEC (Brun et al., 2008). In a CANN model, the spatial period of grid fields is a function of the mapping of the speed of the rat onto the speed of the activity bump on the toroidal manifold (Samsonovich and McNaughton, 1997; Conklin and Eliasmith, 2005). Because the bump cannot move simultaneously at different speeds, CANN models require that multiple, relatively independent toroidal attractor modules with different spatial scales (bump speeds) are present at different dorso-ventral locations in the MEC, and that the spatial scale of grid fields should change discontinuously. This prediction was recently confirmed by Barry et al. (2007). Combining the output of neurons from multiple toroidal attractor networks with different spatial scales would create a distributed code for position. Such a distributed code is similar to a modulo representation of numbers, and allows a larger capacity with fewer neurons than a sparse, unary-like code (Fiete et al., 2008). This position code can then be translated into a more sparse code such as the one in CA3 by, for example, summation of inputs from grid cells at multiple scales (McNaughton et al., 2006; Solstad et al., 2006).

The average tuning curves of place cells and grid cells are usually depicted as smooth firing rate distributions in space, which are easily modeled with attractor networks; however, this smoothness is actually an artifact of trial averaging. The firing of place and grid cells is sensitive not just to location, but also to the phase of the theta oscillation (a 4–12 Hz rhythm recorded in the local field potential of the hippocampus and MEC). The firing of a place cell on a single pass through its average firing field consists of a series of brief bursts of spikes, with an interburst frequency slightly higher than the theta oscillation (O'Keefe and Recce, 1993; Maurer et al., 2005). This results in theta phase precession, such that, as the rat enters a place field, the spikes occur at the trough of the theta oscillation, and then shift earlier and earlier in phase upon progression through the field, until the spikes have moved through 360° (but never more), when the rat exits the field (O'Keefe and Recce, 1993). Theta phase precession has also been observed in Layer II grid cells (but not in most layer III conjunctive cells; Hafting et al., 2008). Phase precession has been hypothesized to play a role in storing and possibly predicting temporal sequences of activity (Jensen and Lisman, 1996; Skaggs et al., 1996; Wallenstein and Hasselmo, 1997; Buzsaki, 2006; Lisman and Redish, 2009). Thus, it is important that a model for grid cell activity can also show phase precession. Previous attractor models of place cells have shown that the activity bump can widen and narrow during a theta cycle, thus showing a small amount of phase modulation of place cell firing rates, but not phase precession as is observed experimentally (Samsonovich and McNaughton, 1997; Conklin and Eliasmith, 2005).

At the time of their discovery, O'Keefe and Recce (1993) proposed that phase precession is generated by the sum of two oscillators of slightly different frequencies: theta, and an intrinsic oscillation frequency of the neuron. This interference pattern gives rise to an envelope (the place field) whose frequency is the difference between the two basis frequencies. The peaks within that envelope shift in phase progressively earlier relative to the lower frequency component (theta). This oscillatory interference model, as an explanation for the generation of place fields, encounters difficulty with some of the properties of CA1 pyramidal cell phase precession (for discussion see Maurer and McNaughton, 2007). The model, however, also predicts periodicity of firing fields, and since the discovery of grid cells, has been extended (O'Keefe and Burgess, 2005; Burgess et al., 2007; Burgess, 2008) to a two dimensional model that appears to account very well for some properties of the MEC grid cell network. The implementation of this model with currently known cell types, however, requires maintaining oscillations of different frequencies within electrically compact cells such as MEC stellate cells, and this has been shown to not be biophysically plausible (Remme et al., 2009).

An orthogonal class of explanation for phase precession was proposed by Tsodyks et al. (1996) and by Jensen and Lisman (1996; see also Wallenstein and Hasselmo, 1997). In these models, neurons respond at different locations along a 1D track by virtue of differential synaptic inputs driven by external cues. Repeated traversal of the track (or some other unspecified process) results in asymmetric intrinsic connections via Hebbian strengthening of connections in the forward direction (called a "phase sequence" by Hebb, 1949). Phase precession in these asymmetric connection models results from dynamics in which the external input is enabled at the beginning of each

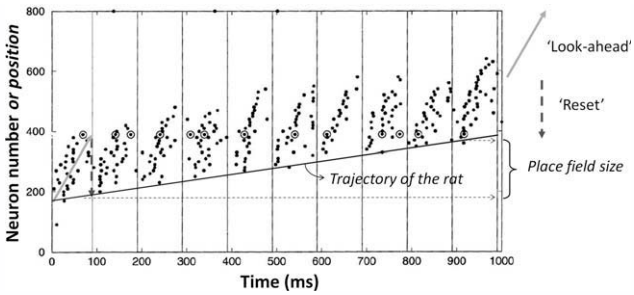

FIGURE 2. Tsodyks et al. (1996) model of phase precession. Simulation of 800 neurons, arranged along the y-axis according to the position of their firing maxima along the rat's 1D route. Time is represented along the *x*-axis, partitioned into theta cycles. The spikes of neuron #400 are circled. At the beginning of each theta cycle (vertical line), external input activates the neurons corresponding to the rat's current location. Then assymetrical connections propagate neural activity to neurons representing positions ahead of the rat ("look-ahead"). The activity is "reset" back to the current location of the rat at the beginning of the next theta cycle. Thus, neuron #400 fires spikes late in theta phase upon entry into its field, and early in phase when the rat is exiting the field. The size of the place field is the distance moved in space from the first to the last spike (adapted from Tsodyks et al., 1996). Note that, in the Tsodyks et al. model, the reset is assumed to be governed by external cues, and the connection asymmetry that underlies phase precession is in the recurrent connections of the place cell network. Both of these assumptions are incompatible with path integration in multiple directions. The present model was devised to overcome these problems.

theta cycle and then gated off, allowing the asymmetric intrinsic connections to activate a short sequence of neurons coupled to locations ahead of the animal. Accumulating inhibition interrupts this process at the end of the theta cycle, and a new cycle begins with external input reflecting the new actual position of the rat. This mechanism generates phase precession, because the cells that fire at the beginning of the theta cycle are those that are activated by external cues at the current position of the rat, whereas those that fire later in the cycle reflect locations ahead of the rat. During each cycle, there appears to be a time-compressed prediction (Skaggs et al., 1996) of the sequence of place fields through which the rat will move ("look ahead"), followed by a "reset" to the actual position of the rat at the beginning of the next theta cycle. This is illustrated in Figure 2, which is adapted from Tsodyks et al. (1996). There are two main shortcomings of the asymmetric connection models of phase precession. First, phase precession occurs omnidirectionally during 2D foraging behavior, such that the first spikes fired on entry to the field are at late theta phase, regardless of the direction from which the rat enters the field (Burgess et al., 1994; Skaggs et al., 1996). This implies that the network must be able to "look ahead" or predict the sequence of place fields ahead of the rat in all directions, and thus there cannot be asymmetry in the recurrent connections. The second problem is that place fields can be updated solely by path integration, in the absence of sensory cues (McNaughton et al., 1996) which means that the mechanism controlling the "reset" of activity every theta cycle cannot depend solely on external cues.

We describe here a neural network model of grid cells, which shows phase precession and addresses the problems with previous network models of precession. We use a network with connectivity forming a ring attractor (a 1D version of the toroidal attractor connectivity in Samsonovich and McNaughton, 1997). Conjunctive cells in this model fire specifically to a heading-direction and drive the asymmetrical look-ahead of the grid cell network. Additionally, because, in the toroidal attractor map the relative distance between the firing nodes of different cells (spatial phase) is predetermined by their connectivity, the reset of the bump every cycle does not need to be implemented by an external input, but instead can be controlled by intrinsic dynamics of the network and neurons. We suggest that a reset of the network bump of activity may result from intrinsic conductances of stellate cells in layer II of MEC, which show intrinsic medium after-hyperpolarization (mAHP) and after-depolarization (ADP) peaks approximately 20 ms and 100 ms following a spike, respectively (Klink and Alonso, 1993). These phenomena could cause the jump-back of the bump at the start of each theta cycle, because they would allow neurons active a set time ago (~100 ms) to reinitiate activity during a lull in synaptic inputs. Such a mechanism has been suggested for short-term memory maintenance over one theta cycle (Lisman and Idiart, 1995; Jensen and Lisman, 1996). We simulate this proposal in a network of integrate-and-fire neurons with a conductance decrease for the mAHP and conductance increase for the ADP, implemented after every spike. Finally, we present a reanalysis of data (Giocomo et al., 2007) on intrinsic currents of MEC neurons, which provide empirical support for the postspiking dynamics of the stellate cell membrane assumed in our model.

RESULTS

Simulations

A network of integrate-and-fire neurons with connections forming a ring attractor was implemented. The network included 100 simulated grid cells, and 200 conjunctive cells, half representing movement in the "north" direction, and half in the "south" direction (see Figs. 1A,B). The north conjunctive cells were activated with a constant input (we assume coming from "north" HD cells), of an amplitude proportional to running speed. All conjunctive cells also included a sine wave input at 8 Hz, to simulate the theta rhythm. Grid cells included after-spike conductances resembling the medium after-hyperpolarization (mAHP) and after-depolarization (ADP) of MEC stellate cells (see Methods) and received input from the simulated conjunctive cells and other grid cells. A single run of the model with HD input of 6 mV, an ADP conductance peak time of 130 ms, and an NMDA fall time constant of 150 ms is illustrated in Figure 3A. An activity bump was

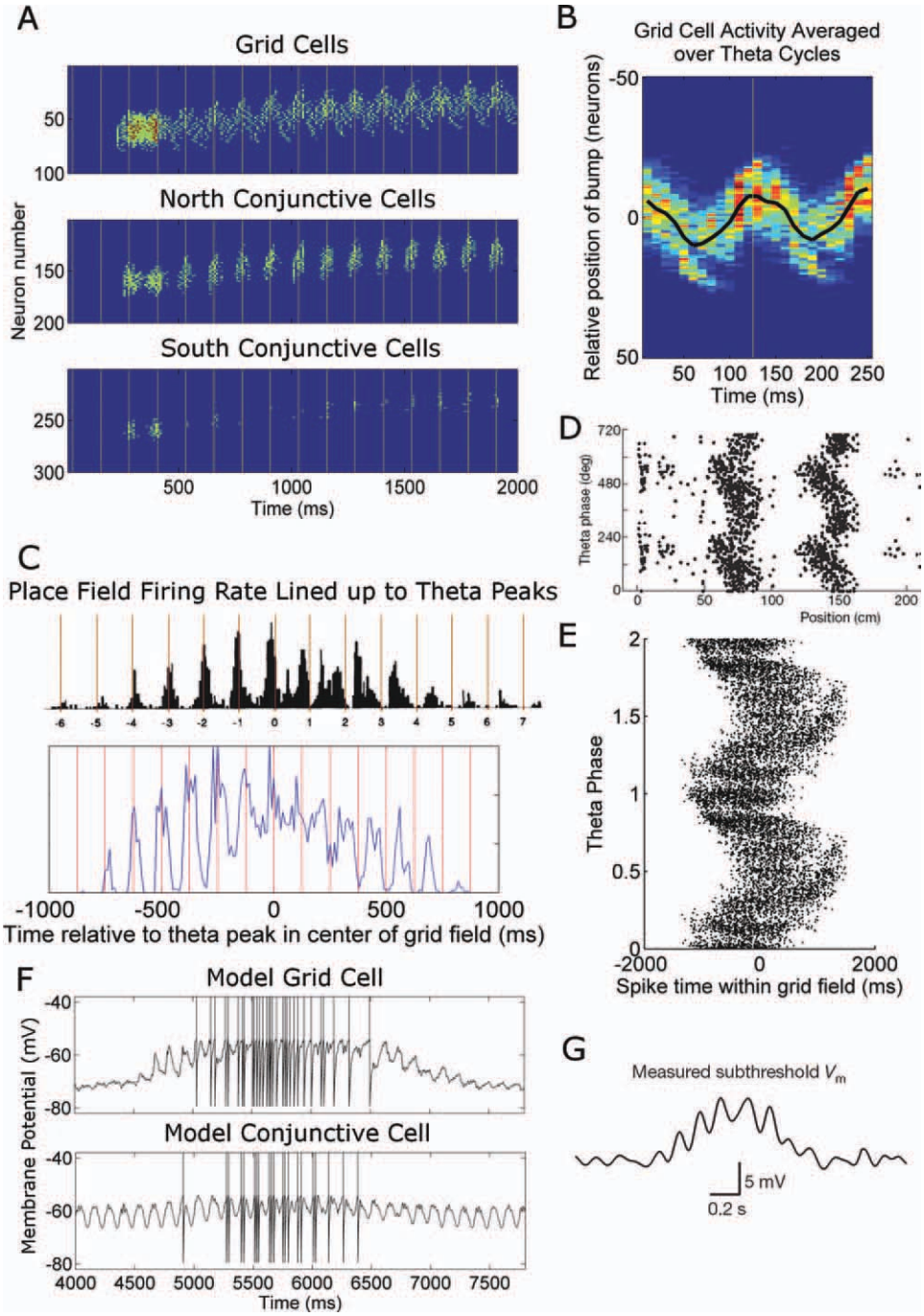

FIGURE 3. Grid and conjunctive cell network simulation. A: General behavior of the model. The activity of all simulated neurons (*y*-axis) during 2 s of simulation is displayed. Spikes are binned into 10 ms bins, with time displayed along the *x*-axis. B: The average activity of grid cells in every 2-theta cycle period was calculated. The center neuron of the grid cell activity bump was calculated for every 2-theta cycle period and used to line up and average together all of the 2-theta cycle intervals in the simulation. The average normalized position of the bump in each 10 ms time bin is marked by the black line. C: All firing fields were aligned according to the theta peak at the center of the field, to determine the probability of spiking in each 10 ms bin (bottom plot). Compare simulation results (bottom plot) to same analysis of a CA1 place field from Skaggs et al. (1996) on top plot. In both plots, red lines mark theta peaks, which refer to the phase of theta during which the cells exhibit maximal firing (this is the trough of the theta oscillation measured in the pyramidal cell layer for CA1 cells). D: Theta phase precession of MEC grid cells recorded by Hafting et al. (2008). E: Model grid cell spikes are plotted according to the theta phase and time relative to the center of the field in which they occurred. F: Membrane potential traces of one simulated grid cell and its corresponding conjunctive cell, showing a pass through 1 grid field. G: Patch clamp data from Harvey et al. (2009), showing the theta filtered membrane potential of a mouse CA1 cell during a pass through the cell's place field in a virtual environment. Note that the size of theta oscillation peaks increases within the place field, as they do in our model grid cells. [Color figure can be viewed in the online issue, which is available at wileyonlinelibrary.com.]

TABLE 1.

Synaptic Weight Parameters Used in the Simulations

	Max excitatory weight	Spread (neurons)	Offset (neurons)	Inhibitory weight
Grid -> grid	0.0256	15	0	0.0617
Grid -> conjunctive	0.0473	10	0	0.0167
Conjunctive -> grid	0.0786	6	11	0.0167
Conjunctive -> conjunctive	0			0.0222

Excitatory synaptic weights between the neurons were assigned as a function of distance between the neurons (along the ring attractor). The maximal weight, spread (standard deviation) of the Gaussian distribution that determined the weights (in number of neurons), and offset (in number of neurons) are shown. The resulting weights between all neurons are displayed in Figure 1B. Global inhibition was implemented as an inhibitory connection with a delay, between all excitatory neurons. The weights of these inhibitory connections are displayed in the last column. All weights are unitless quantities which represent the peak conductance of the channels (AMPA or GABA) multiplied by the resistivity of the cell membrane. For comparison, an excitatory connection of 0.0143 raises the membrane potential from rest (−70 mV) by ∼1 mV. An inhibitory connection of 0.1 decreases the membrane potential from rest by ∼1 mV.

activated at a random location on the ring attractor. As a result of the "theta" input, conjunctive cells were only active during a portion of the theta cycle corresponding to the peak of this input, and hence, consistent with the data of Hafting et al., (2008) for layer III MEC cells, did not exhibit full phase precession. During the firing of conjunctive cells, the activity bump in the grid cell layer moved in one direction ("look-ahead"). At the theta input trough, a lack of inputs and continued inhibition caused the bump to collapse. The ADP and synaptic NMDA conductances helped the bump to reform at (or "jump-back" to) the group of cells active ∼110 ms previously. Thus, as a whole, the grid cell population was active for most of the theta cycle, with the focus of activity sweeping forward and increasing in intensity up to the peak of theta, and then waning and jumping back towards its point of origin during the theta trough. The average bump movement within a cycle is shown in Figure 3B.

As a result of the look-ahead and partial jump-back of the activity bump during each theta cycle, each grid cell fired at successively earlier theta phases during progression through the active grid field (Fig. 3C). The shape of the theta phase precession plot (Fig. 3E) depended on the dynamics of the bump look-ahead (Fig. 3B). Two factors contribute to the shape: early in the theta cycle, grid cells reinitiated spiking as a result of the ADP and NMDA currents, and late in the theta cycle, new grid cells were activated by conjunctive cell activity. Activation by ADP currents was less precisely timed than the inputs from conjunctive cells, resulting in reduced phase selectivity towards the end of the field (where spikes occur in the early part of the theta cycle), as is seen in experimental place cell and grid cell data (Fig. 3D). This is also seen in plots of fields aligned to theta peaks (Skaggs et al., 1996; Fig. 3C). In this plot, spikes are binned into several time bins within each theta cycle. Many passes through the field are then aligned based on the theta peak that occurs in the center of the field, so that the theta phase in which spikes occur in each theta cycle throughout the field can be visualized. Firing rate peaks at the beginning of the field, occur late in theta phase, and are sharper than the peaks at the end of the field, which occur early in theta phase. As in the experimental data, in the middle of the field, two peaks tend to occur in one theta cycle. In the model, this was because in the middle of its grid field, the cell may become activated by both conjunctive cell activity and ADP currents. The precise shape of the look-ahead and jump-back (and thus the phase precession) depended on the precise intrinsic conductances and time constants as well as synaptic weight parameters, which are not known for *in vivo* networks. The synaptic parameters used in all simulations shown were chosen because they resulted in fairly realistic phase precession, but also because they allowed the bump activity to be robust enough to allow some manipulation of inputs and time constants (see below). The parameters used here are in Table I. Simulations with different synaptic weight parameters showed, for example, a more discontinuous jump-back than is displayed here.

The membrane potential (and spikes) of a model grid cell and a conjunctive cell during a pass through a grid field are displayed in Figure 3F. The membrane potential of conjunctive cells is theta modulated throughout the simulation, as a result of the constant head direction inputs. Grid cells only show strong theta modulation of the membrane potential during a pass through a grid field, when the inputs from conjunctive cells are strongest. This is similar to the theta modulation of the membrane potential of a CA1 place cell during a pass through its place field (Harvey et al., 2009; Fig. 3G).

To simulate changes in grid scale along the dorsal-ventral axis of the MEC, the time constants of the mAHP and ADP were varied (Fig. 4A). Increasing the time constants caused reinitiation of spikes to occur later, increasing the interburst interval of the grid cells (as measured from the autocorrelogram; Fig. 4B). As a result, the neurons that were likely to reinitiate during the lull of input at the theta trough were the ones that had been activated earlier in the last theta cycle,

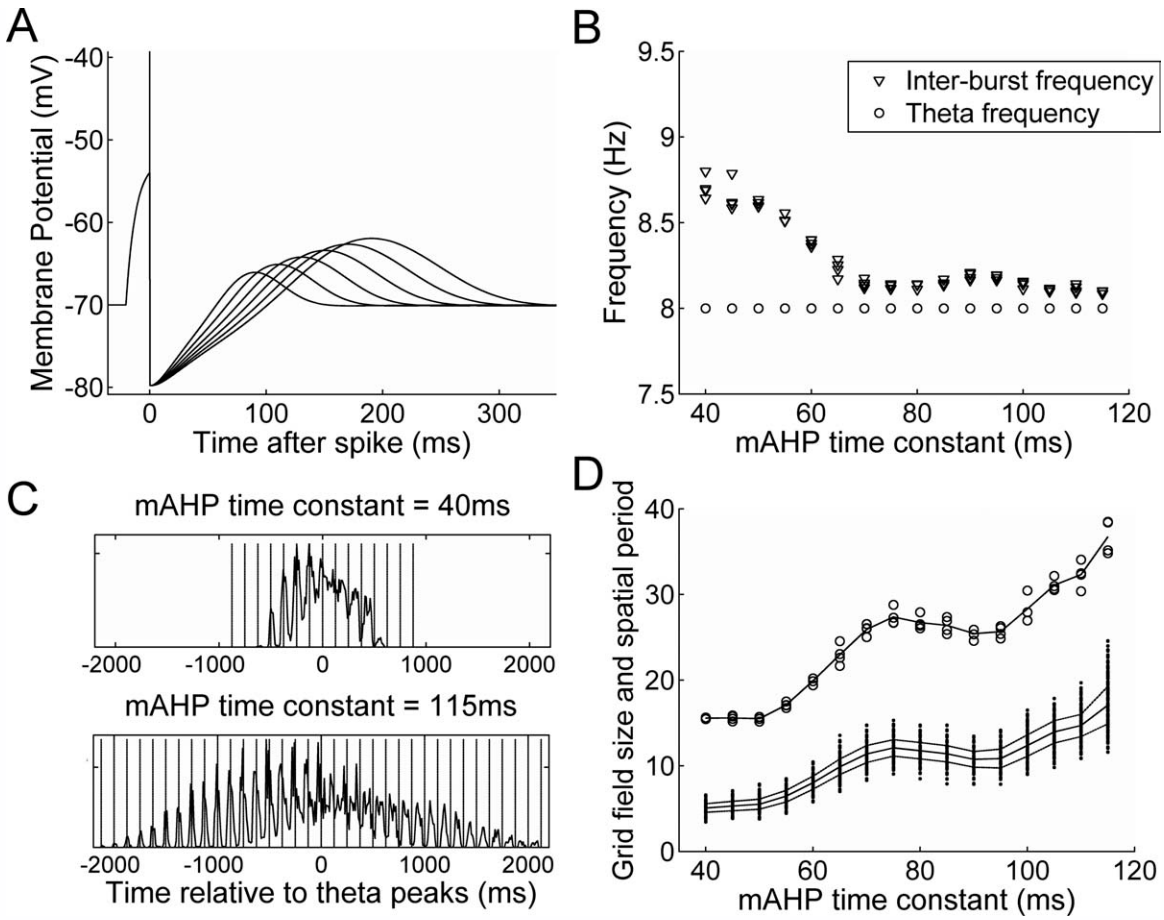

FIGURE 4. Variation of after-spike conductance time constants in grid network simulations. A: Variation of the mAHP and ADP conductance time constants resulted in the after-spike potentials shown. All time constants (mAHP time constant, ADP peak delay and ADP peak width; see Methods), were varied proportionally. The mAHP time constants shown are 40, 50, 60, 70, 80, and 90 μs. The strength of the ADP current was increased with an increase in time constants, to keep the firing rates of grid cells during a run of the full simulation constant. B: Intrinsic burst frequency (as measured from the autocorrelation) of grid cells in network simulations run with various after-spike conductance time constants. Theta frequency (frequency of head-direction input to conjunctive cells) was set to 8 Hz in all simulations, and all other parameters were also unchanged. C: Firing within grid fields aligned to theta peaks (red lines) in simulations run with mAHP time constants of 40 and 115 μs. With an increasing time delay, simulated grid cells show a slower rate of phase precession, and are active for more theta cycles, resulting in larger grid fields and spatial periods. D: Grid field size and spatial period (in arbitrary units) in simulations run with varying after-spike conductance time constants. Field size (dots) is measured as the time from first to last spike within one field, converted to space units by taking the amplitude of the head-direction input as proportional to running speed. The sizes of all grid fields in each simulation are plotted, along with the average (solid line) and standard deviation (SD) (dotted lines). Grid field spatial period (circles), the distance between grid cell firing peaks, is plotted for each simulation. Several 15-s simulations were run and are plotted for each ADP time delay.

which increased the jump-back size. This resulted in each grid cell firing for a larger number of theta cycles, and a slower rate of theta phase precession (Fig. 4C), and thus increased the grid period and firing field size (Fig. 4D). Because synaptic inputs also played a large role in the timing of spikes, however, the burst frequency was not completely determined by the ADP delay. The interburst frequency changed more slowly than the peak of the ADP, staying faster than theta frequency even if the ADP delay was slower than theta (Fig. 4B). This shows that network connectivity (synaptic inputs), alter, but do not eliminate, the effects of the time constants of intrinsic currents on spike timing. Fernandez and White (2008) have shown that the intrinsic oscillations in stellate cells in vitro are reduced by *in vivo*-like synaptic conductances. In our model, there is a lull in synaptic input to grid cells from conjunctive cells at the theta trough. This may have the effect of unmasking the ADP from the otherwise strong synaptic conductances, and allowing it to cause a "jump-back" of the bump during the theta trough. The fact that the ADP works in this way in the model, suggests that currents which in vitro produce strong oscillations can have significant, though much reduced, effects on interburst frequency *in vivo*. The oscillations observed in vitro, like the time constants of the ADP implemented in our model, are slower than the theta frequency measured in behaving animals

(Giocomo et al., 2007), also suggesting that the *in vivo* level of synaptic conductances acts to speed up the interburst frequency of these neurons.

The other factor that had a large effect on grid field sizes was the time constant of the simulated NMDA current. Without a long-lasting component to the synaptic connections between grid cells, grid cells would not stay active for more than one theta cycle, and thus no phase precession would occur. As the ADP was not strong enough to initiate spiking by itself, depolarization from another source was needed to cause a jump-back. The long-lasting effects of the NMDA currents provided this depolarization in the simulations. Increasing the NMDA time constant (Fig. 5A) increased grid field sizes and the spacing between grid fields (Fig. 5B). This increase was observed even though the synaptic strength of the NMDA component was decreased to keep firing rates constant. The longer-lasting depolarization allowed the jump-back to return to neurons activated earlier in the previous cycle, and allowed each grid cell to be active for a larger number of theta cycles. Changing both the mAHP/ADP time constants and the NMDA time constant together, provided a more than six-fold possible variability in grid spatial periods (Fig. 5C). Even though we have modeled these prolonged synaptic currents as NMDA currents, other prolonged currents, such as the kainate currents found in layer III neurons (West et al., 2007), could instead contribute to phase precession and to determining grid field size. Our results with NMDA and ADP time constants suggest that multiple factors may be responsible for the change in spatial scale in different parts of the MEC.

While the time constant of the H-current increases from dorsal to ventral MEC, it is not clear whether it changes discontinuously, so that the mAHP would be the same for all neurons within an attractor module of a particular scale, as we have so far assumed. In fact, it appears that mAHP at similar dorsal-ventral MEC locations may be quite variable (see below, Fig. 8). To ascertain that the model can tolerate different mAHP time constants between cells within the same attractor module, the mAHP (and ADP) time constants were varied between cells within a grid cell network. The mAHP time constant for each grid cell was chosen randomly from a uniform distribution in a range of 20 ms (and the ADP time constants were changed in proportion to this value for each cell). These simulations showed that, while different values of the mAHP (and ADP) time constants changed the firing rate of individual cells within the grid cell network (in a range of about 5–10 Hz), the field sizes of individual cells varied by at most 20%, and this variability showed no relationship with the time constants of the individual cells. The grid field size and spacing changed as a function of the average mAHP time constant of a given attractor module, but did not change within single modules (Fig. 6A). We further varied the NMDA time constant within an attractor module (in a range of 100 ms), to ascertain that this parameter can be heterogeneous as well. In this case, the firing rates of individual cells varied linearly with the time constant, covering a range of about 4–12Hz, and the field size varied by about 15%. Again, the variability in grid field sizes between grid modules is a lot larger than the variability within a module, even though the time constants overlap significantly between modules (Fig. 6B). This shows that field size is determined by not just the intrinsic properties of the cell, but by

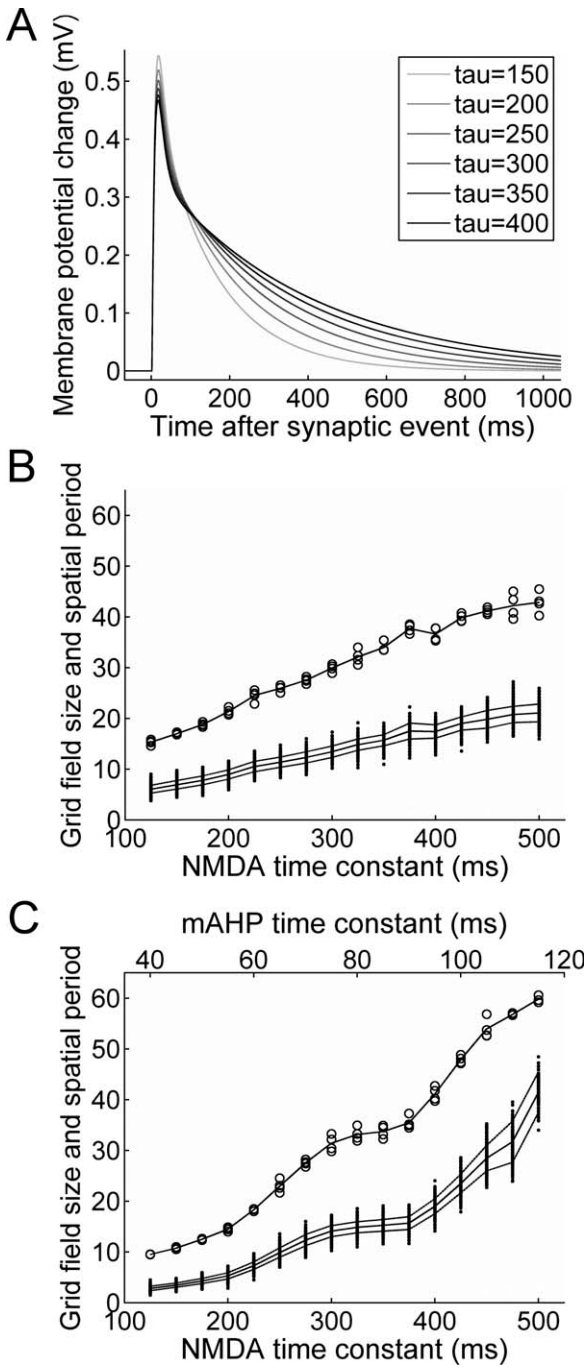

FIGURE 5. Variation of NMDA time constants in grid network simulations. A: Excitatory postsynaptic potentials (AMPA and NMDA component) resulting from different NMDA time constants are shown. The NMDA conductance is decreased as the time constant is increased, to keep firing rates of grid cells constant. B: Increasing NMDA time constants in the simulated grid neurons increased grid field size and spatial period. C: By changing both NMDA and mAHP/ADP time constants, grid field size, and spatial period varied by more than six-fold.

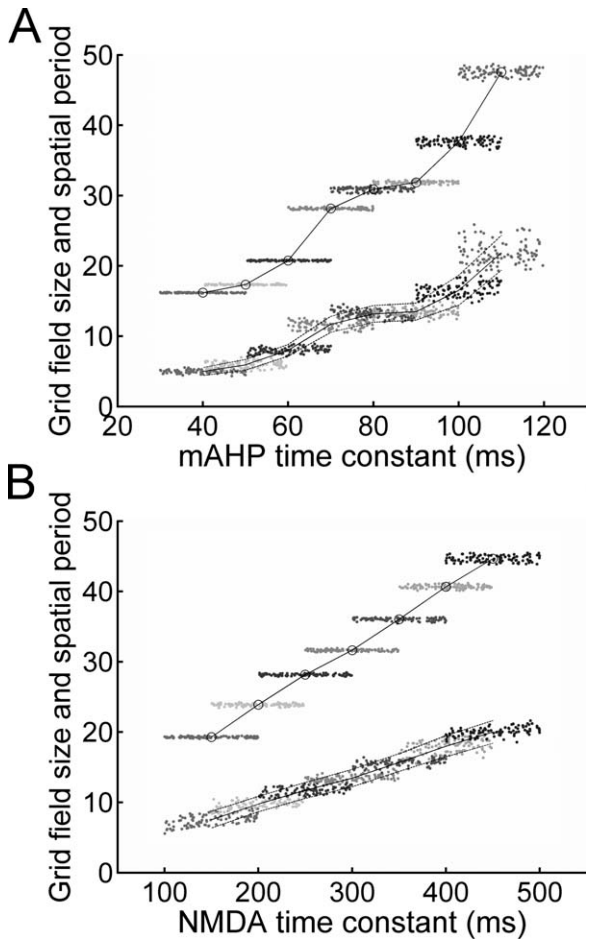

FIGURE 6. Heterogeneous mAHP and NMDA time constants within grid network modules. A: The mAHP and ADP time constants of individual grid cells were varied within each interconnected network. The average grid field size and spatial period of each individual neuron (over a 50s simulation) is plotted according to the mAHP time constant of that neuron. Each separate simulation, representing a different grid module, had a different average mAHP time constant, but the distribution of time constants overlapped between simulations. Each simulation is plotted in a different color, showing that the field sizes showed almost no overlap between simulations, and no relationship with time constant within simulations. B: The NMDA time constant of individual cells within a single simulation was varied. Plotting the field sizes and spatial periods of individual cells according to the NMDA time constant shows that the field size varies much more between network modules (different colors) than within each single module, and spatial period is the same between cells within a module.

the inputs it receives from other cells. The spacing between fields especially, is a function of the average NMDA and mAHP time constants of all the cells in the interconnected network.

Head-direction (HD), grid and conjunctive cells in MEC all increase their firing rates with velocity (Sargolini et al., 2006). To simulate changes in rat velocity, the amplitude of the HD input was varied. Thus, we assume that self-motion signals provide input to the conjunctive cells (possibly via HD cells). Increasing the HD input caused a linear increase in the firing rate of the conjunctive cells (Fig. 7A). Increased conjunctive cell firing caused the grid cell activity bump to move faster (Fig. 7B). This relationship was linear up to an input of about 7.5 mV (Fig. 7C), indicating that the amplitude of the HD input can be used to link rat speed to bump movement through network states precisely in relation to actual movement in space. Extrapolating this relationship showed that no net movement of the activity bump would occur (which would correspond to the rat being motionless) when conjunctive cells receive a HD input of about 0.6 mV. Although this level of input was not enough to sustain a bump of activity for longer than half of a second, other mechanisms, perhaps reduced feed-forward inhibition, which was not simulated here, may sustain the bump when the rat is motionless. The HD input minus the 0.63 mV intercept was used as the rat speed (in arbitrary units) to calculate the field size and periodicity (in arbitrary space units) from the time spent in each grid field (time between first and last spike). Using this spatial scaling factor conversion from rat speed to bump speed kept the spacing between grid field nodes constant across simulated running speeds (Fig. 7D). The spatial scale of course depends on the time constants of grid cell currents (Figs. 4 and 5), but also on the gain of the input from self-motion signals (Terrazas et al., 2005). Information about the gain of the self motion input relative to the actual velocity of the rat (slope and intercept determined above), is all that is needed to keep the spatial scale constant across velocities.

Unlike the spacing between grid nodes, grid field size is determined by the jump-back of the activity bump in each theta cycle. This is because the first spike when entering the field occurs at the end of the look-ahead of the activity bump during that theta cycle (just before the jump-back), and the last spike when exiting that field occurs just after the jump-back in the last theta cycle in which this cell is active (see Fig. 2). Thus, the average distance moved in neural space from the beginning to the end of a grid field is equal to the number of neurons over which the jump-back occurred, and the distance the rat has moved in actual space over this time is the jump-back multiplied by the spatial scaling factor. Thus, in order for grid field sizes to stay constant, the jump-back must not change. However, this is not guaranteed to be the case as inputs to the grid cells change with increased velocity. Thus, the grid field size may change, even though the spacing between grid nodes does not change, altering the proportion of the spacing between grid nodes in which the cell fires. In the simulations, the jump-back, and thus the proportion of spatial period in which a grid cell fired, increased slightly with HD input (Fig. 7D). This effect was stronger or almost absent, depending on the connection strengths between simulated neurons (alternate connection strengths were simulated but are not shown). The connection strengths modulated the jump-back and the intrinsic oscillation frequency of the neurons, even though the time constants of the ADP and NMDA currents were constant. Thus, these connection strengths could be tuned in order for the network to have appropriate field sizes, and to respond to changes in the HD input so that field sizes did not change

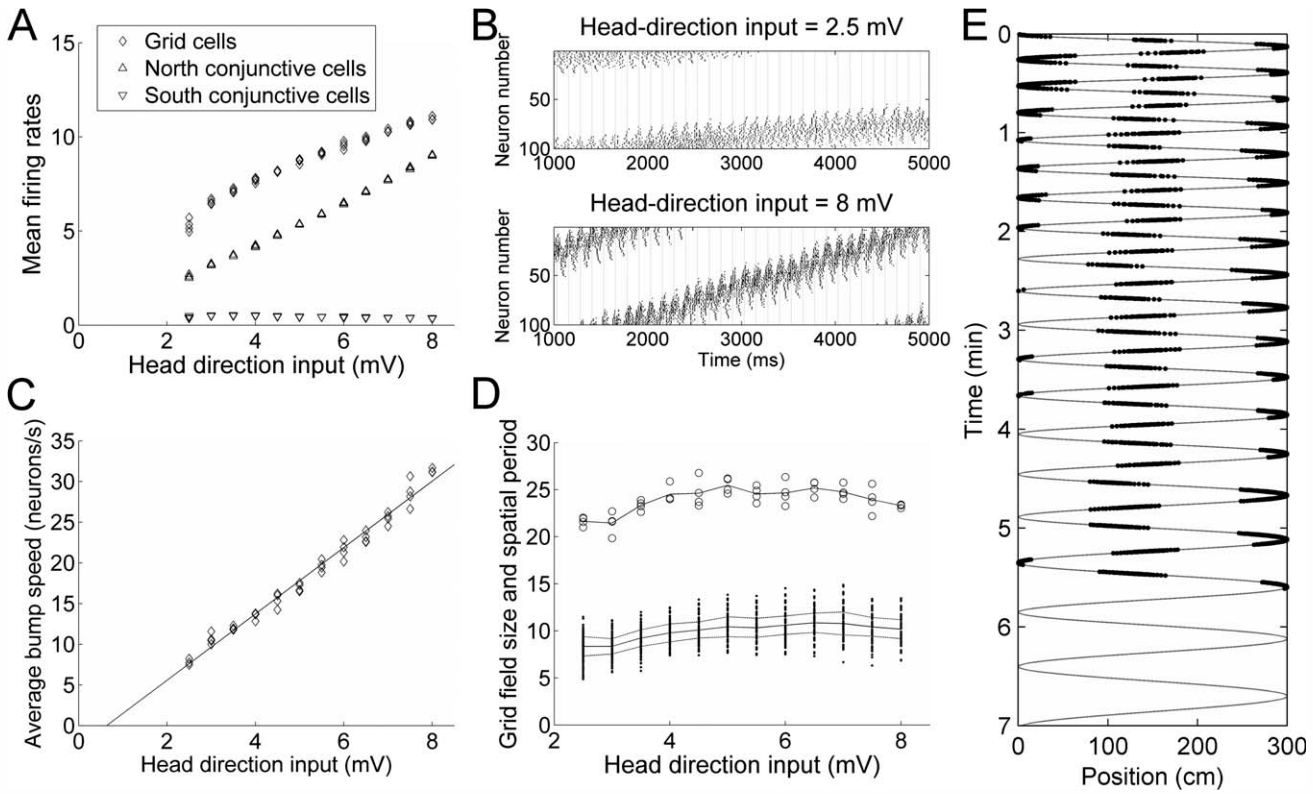

FIGURE 7. Variation of head-direction input in grid network simulations. A: The amplitude of the HD input to the "north" conjunctive cells was varied to simulate different running speeds, resulting in a linear variation of the firing rates of the conjunctive cells and grid cells. B: Examples of bump movement at the lowest and highest HD inputs analyzed. C: The average slope of movement of the grid cell activity bump varied linearly with HD input. HD inputs with amplitude lower than 2.5 mV did not sustain an activity bump for longer than 4 s. D: Grid field size and spatial period as HD input was varied. The linear fit of the relationship between HD input and average bump movement (in C) was used as the spatial scale to convert the time of neural activity to the space covered in the environment (in arbitrary units). E: A single simulation run with varying velocities and directions. The simulated path is plotted in gray. The path simulated running along a linear track as a sine wave, with the frequency of the sine wave (speed of running each lap) decreasing over laps. The spikes of a single neuron in the simulation are plotted along the path. Field size decreased slightly over laps (increased with velocity). There was some random drift in the movement of the activity bump, resulting in slight shifts of field locations over laps. After a long period of low inputs (at the turn around point during a slow lap), the bump collapsed, and thus the firing of all cells stopped (see text).

with it. Alternately, the jump-back (and thus field size) could be kept constant with HD input by decreasing the ADP time constants as the HD input was increased (data not shown). Ion channels including the H-channel change their open time constants with depolarization (Dickson et al., 2000; Giocomo and Hasselmo, 2008), and thus the time constant of the ADP and mAHP may actually change with increased input to the neurons, resulting in constant grid field sizes. We tested this possibility in slices of MEC by measuring the time constant of the mAHP at different depolarized potentials (see below).

Finally, to determine if correct path integration would occur in a longer simulation at varying speeds, a path of back and forth movement along a linear track was simulated. The simulated track was 300 cm long, and the simulated movement was a sine wave (thus slowing down at either end of the track), with the time to travel each lap decreasing across laps. The velocity required to travel along this path was used as an input to the model, converting velocity (in cm/s) to a head-direction input (in mV) by dividing the velocity by 7 (arbitrary factor chosen to allow the simulation to represent the speeds at which rats commonly run; McNaughton et al., 1983) and adding the baseline input (0.63 mV) at a bump speed of 0, as determined above. This simulation showed that the model could perform path integration even when velocity varied. The spikes from one simulated grid cell are plotted on the simulated path in Figure 7E. There was some random drift in the bump position integrated by the model, with error accumulating at up to 10 cm/s, which is ~15% of the size of the grid fields simulated per second or 6.5% of the spatial period per second. The only condition in which the error became systematic was at HD inputs of over ~8mV, where the neural activity bump started moving nonlinearly faster than the input.

This simulation of back-and-forth running also shows some interesting predictions for grid fields in multiple directions of travel. As a result of the mAHP, once a grid cell starts firing, it continues firing in future theta cycles, regardless of the rat's new running direction. Thus, if the rat turns around in the middle of a field, the look-ahead activates cells ahead of the rat

in the new direction, but the jump back only activates cells that were activated previously, not the cells directly behind the rat. In a 2D environment or simulation, this may be seen as a sequence of cells activated in a single theta cycle that represent positions in the same path the rat took, such as around a corner, and not in a straight line. In the hippocampus, such a phenomenon is observed when a rat turns around on a linear track within a place field. Place cells that are otherwise unidirectional on a linear track exhibit bidirectional firing when the rat turns around within the cell's place field, indicating an 'inertia-like' process (Redish et al., 2000), such as the ADP in this model, which predicts a jump-back to previously activated cells, regardless of what is directly behind the rat at the current time. In our 1D simulations, neurons that were activated for just one or two theta cycles before the turn around point, are not activated again in the reverse direction, because they were not active strongly enough for the jump-back to reach them (data not shown). In contrast, the interference oscillator model predicts symmetrical grid fields in both running directions. The current model shows a look-ahead that is longer than the jump-back, resulting in grid fields that are shifted in the forward running direction, and thus asymmetrical in the two running directions (Fig. 7E).

Analysis of mAHP Timing in MEC Stellate Cells

To test the hypothesis that after-spike potentials vary with the scale of grid fields, we analyzed the mAHP in layer II stellate cells (a subset of the cells whose membrane properties were reported by Giocomo et al., 2007). The time constant of the mAHP differed in layer II stellate cells along the dorsal-ventral axis of MEC. Figure 8A shows examples of the mAHP from different dorso-ventral levels, when the membrane potential was approximately −50 mV (between −53 and −48 mV). As determined by the Kolmogorov-Smirnov test, the stellate cell mAHP time constant was significantly shorter in dorsal MEC (dorsal mean $\tau \pm$ standard error of mean (SEM), 53.3 ± 4.8 ms and $n = 16$;) compared to ventral MEC (ventral mean $\tau \pm$ SEM, 70.5 ± 5.7 ms and $n = 15$; $P < 0.01$) at an approximate membrane potential of -50 mV. The time constant showed a range of 86 ms (from 32.6 to 118.9 ms) and systematically increased from dorsal to ventral portions of MEC at multiple membrane voltages (−55 mV: $r = 0.56$, slope = 17.7, $P = 0.3263$ and $n = 5$; −50 mV: $r = 0.56$, slope = 23.1, $P < 0.05$ and $n = 31$; −45 mV: $r = 0.71$, slope = 26.1, $P = 0.06$ and $n = 11$; Fig. 8B, left). The mAHP time constant did not significantly correlate with cell resistance ($R^2 = 0.0004$) or firing threshold ($R^2 = 0.004$).

To test if the model could reproduce the range of experimental data that has been recorded, the experimentally determined changes in grid spacing and mAHP over dorso-ventral locations in MEC were compared to the modeled results. In the supplemental material of Sargolini et al. (2006), the gradient in grid spacing along the dorso-ventral axis of the MEC was fit with the following equation provided by T. Hafting:

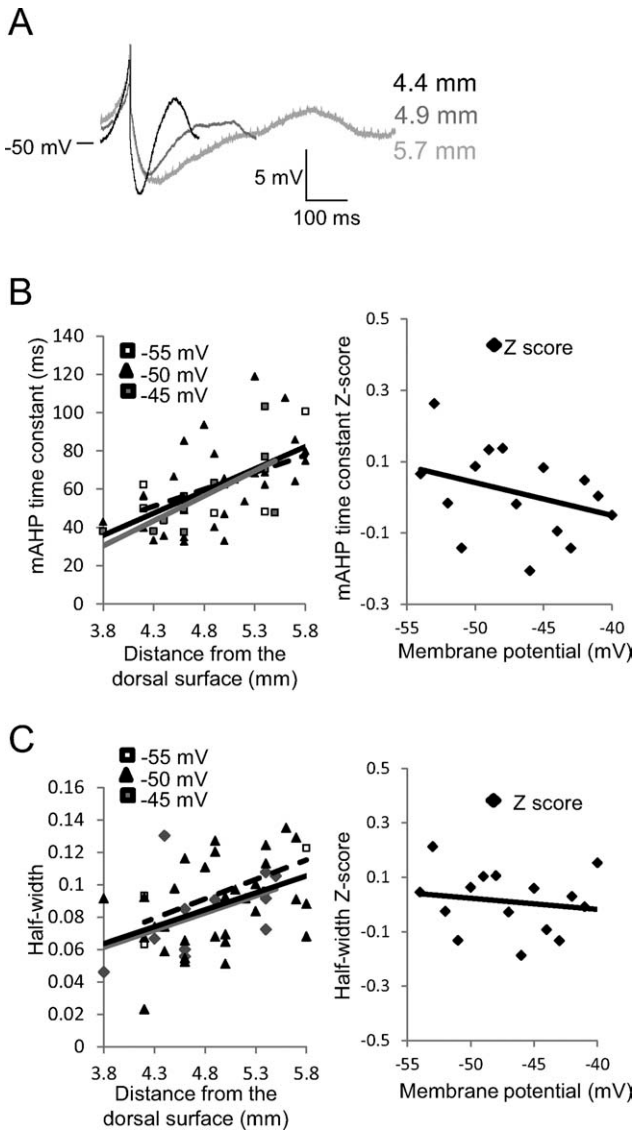

FIGURE 8. After-hyperpolarization in stellate cells along dorso-ventral axis of the MEC. A: Examples of the mAHP after a single action potential at an approximate membrane potential of −50 mV. Faster time constants for the mAHP were observed in more dorsal portions (black) compared to more ventral portions (gray) of MEC. B: The recovery time constant of the AHP increases along the dorsal ventral axis of MEC at multiple membrane potentials (left). The recovery time constant of the AHP shows a slight decrease with membrane depolarization (right). C: The half-width of the AHP increases along the dorsal ventral axis of MEC at multiple membrane potentials (left). The half-width shows a slight trend of decreasing with depolarization (right).

$G(z) = 30z + 37.09$ (for grid spacing in cm; z is the distance from the postrhinal border in mm). This indicates that the spacing between grid fields at the postrhinal border is 37.09 cm, and increases by 80.9% every mm. To better compare the gradient in the mAHP time constant to the gradient in grid spacing, the mAHP dorsal-ventral depth was rescaled to indicate the distance from the postrhinal border (at ∼3.8 mm from the surface of the brain). The gradient for all mAHP data

was best fit by the following equation: $\tau(z) = 23.16z + 35.35$ (τ in ms, z in mm). In the model with heterogeneous mAHP and NMDA time constants, the spacing between grid cells started at 13.9 (arbitrary units at mAHP = 40 ms) and increased by 30.5% for every 10 ms increase in mAHP time constant (linear fit to Fig. 6A). Plugging in the experimentally measured relationship between mAHP time constant and dorso-ventral location in the MEC, this would predict a spacing increase of 82.5% every mm. This is very similar to the experimentally determined 80.9% increase; however, different model parameters (including simply removing the heterogeneity of mAHP time constants within a single module of the model; Fig. 4D) greatly change this result. The linear fit to Figure 4D suggests an increase of 42.3% every mm. These results further support the finding that grid field spacing is not simply determined by the mAHP and many other factors contribute. Importantly, however, an identical increase in grid spatial period to that observed in the dorsal-most 1.5 mm of MEC (Sargolini et al., 2006) can be achieved in one version of the model, by simply increasing the mAHP time constant at the same rate as is observed in the same region of the MEC.

In addition to a systematic change along the dorsal ventral axis, the time constant of the mAHP showed a slight decrease with additional depolarization (from −54 mV to −40 mV). To compare the effect of membrane potential on mAHP time constant across multiple cells, the z-score of the time constant was computed at each potential. The time constant for the mAHP decreased slightly with depolarization ($R^2 = 0.13$; Fig. 8B, right). Although the decrease was not significant, a decreasing mAHP time constant with depolarization is consistent with previous research indicating a decrease in the time constant of I_h with depolarization (−50 to −45 mV; Dickson et al., 2000, Giocomo and Hasselmo, 2008; Fig. 8B). The mAHP half-width also increased from dorsal to ventral portions of MEC at multiple membrane potentials (Fig. 8C) and showed a slight trend with depolarization in the same direction as the time constant of the mAHP.

DISCUSSION

The model developed here accounts for the periodic structure of MEC stellate cell firing fields using the Samsonovich and McNaughton (1997) framework with periodic boundary conditions. That model simulated movement of an activity bump on a periodic place cell manifold by driving place-by-head-direction (conjunctive) cells with an input proportional to running speed. Modulation of this input at the theta frequency resulted in fluctuations of the bump speed within a theta cycle, but no explicit 'jump back', and thus no phase precession. To account for phase precession without spatially selective, external input to reset the bump location, we assumed that an intrinsic cellular mechanism renders cells hyperexcitable at a certain postspike latency, so that the bump would reset at the end of the theta cycle to an earlier location on the manifold. The mAHP and ADP observed in MEC stellate cells appear to be good candidates for this mechanism, provided that their timing properties vary appropriately along the dorsal-ventral axis of MEC. Postspike dynamics of MEC stellate cells recorded *in vitro* exhibited time constants and half-widths of the mAHP that increased linearly in the dorsal-ventral direction, with a resulting linear increase in the latency of the ADP. Using the observed parameter values, we found that grid cell dynamics could be simulated rather faithfully, including realistic phase precession, firing over the number of theta cycles observed in dorsal MEC at various running speeds, firing fields that covered about half a grid period, stable grid periods under changes in velocity, and variation in field size and periodicity with changes in mAHP time constant (reflecting dorso-ventral variation in grid characteristics).

We believe that the major advantage of our model is its relatively simple implementation of both network as well as intrinsic current dynamics to achieve path integration and account for phase precession. Previous models of grid cells have focused on either network properties (Fuhs and Touretzky, 2006; Guanella et al., 2007) or intrinsic, single cell properties (e.g., Burgess et al., 2007; Blair et al., 2007) to explain the firing properties of grid cells. Attractor models of path integration are preferable to single cell models, because they are more robust to the presence of noise (see Zilli et al., 2009 for an analysis of the effects of noise on oscillatory interference models). Attractor models of path integration also predicted a priori both the existence of theta-and speed-modulated conjunctive cells in MEC and the quantization of grid scale (McNaughton et al., 2006), neither of which are explicitly called for in alternative models (e.g., Burgess et al., 2007; Kropff and Treves, 2008). Previous models with attractor network dynamics, however, did not account for phase precession (Fuhs and Touretzky, 2006; Guanella et al., 2007). Our current implementation of an attractor network-like connectivity with intrinsic currents expressed phase precession very similar to that observed experimentally in the presence of noise, in contrast to previous grid cell phase precession models (Blair et al., 2007; e.g., Hasselmo and Brandon, 2008), and would theoretically produce omnidirectional phase precession in a 2D implementation, without the need for any external input or resets to correct for noise. Our 1D simulations showed faithful path integration of a varying velocity input over several minutes (Fig. 7E).

All of the basic elements implemented in this attractor network model appear to be present in the MEC, including: the presence of conjunctive grid × HD cells (Sargolini et al., 2006) and their connectivity to the layer II grid cells (Lingenhohl and Finch, 1991; Germroth et al., 1989; reviewed in Witter and Moser, 2006), feed-forward and feedback inhibition, prolonged excitatory currents (West et al., 2007), and afterspike currents that change time constants along the dorsal-ventral axis (shown here). As implemented, the model also posits recurrent connectivity between grid cells. Although recurrent connectivity is more prominent in layer III of the EC (Dhillon and Jones, 2000), it has been observed between layer II stellate cells as well (Kumar et al., 2007). Quantitative consideration of

the torus model suggests that actual connectivity is likely to be very low. In the present simulations we used a Gaussian synaptic weight function; however, in a realistically sized network, the weight function can be replaced by a probability function, with binary weights. In the 1D case, we succeeded in reproducing the dynamics with the equivalent of about 15% connectivity. In a 2D case, the probability would be the square of 0.15 i.e., on the order of 2.25%. Given that there are nongrid cells in layer II, which may or may not have recurrent connections; this fraction may be lower still. Alternately, other network architectures, in which the bulk of the recurrent connectivity would occur between layer III conjunctive cells (possibly a subclass of phase precessing conjunctive cells), could result in path integration and similar properties of grid cells.

This model proposes two causes of grid cell firing under the theta regime: the after-depolarization potential, which causes cells active sometime in the past to become active again, and conjunctive cells, which cause cells in the direction ahead of the rat to fire. As a result of the two different causes for spiking, the model predicts that spikes generated at different phases of the theta cycle (and different locations in the field of a single grid cell), can have different properties, such as precision of timing. Other grid cell phase precession models do not share this prediction; they suggest the same mechanism causes spikes throughout the field and thus predict a constant slope of phase precession (e.g., Burgess et al., 2007; Blair et al., 2007). The distribution of spikes on a theta vs. position plot in fact appears to have a different slope and width at early compared to late theta phases (Skaggs et al., 1996). This also predicts that place fields may be asymmetrical when traversed from one direction compared to the other, as the early field spikes generated by conjunctive cell inputs when the field is traversed in one direction, will be late field spikes generated by the ADP when the same field is traversed in the other direction. In our simulation of back-and-forth running (Fig. 7E), fields are slightly shifted in the direction of running, suggesting that the 'look-ahead' activated by conjunctive cell inputs is longer than the re-initiation of spikes in grid cells via the ADP. Fields of CA1 place cells also appear to be shifted in the forward running direction when traversed from opposite directions (Battaglia et al., 2004).

The two causes of grid cell spiking predicted by this model are also consistent with models that suggest that the hippocampus is involved in prediction of future events and sequence encoding (Buzsaki, 2006, pp. 326–327; Jensen and Lisman, 1996). Spikes generated by the ADP can be thought of as "retrospective," or a cellular "memory" for the rat's location in the past, and spikes generated by conjunctive cells could be "prospective," predicting the location in the future. This mechanism would allow the grid cell network, or a network downstream of it, to strengthen the synapses between neurons representing sequences of visited locations, by repeating this sequence multiple times during a single pass through the locations (Skaggs et al., 1996; Jensen and Lisman, 1996). Finally, an attractor map model of grid cells is consistent with a planning function for the grid cell network and down-stream structures, similar to the one proposed by Hopfield (2010). Hopfield proposes that adaptation in an attractor map would cause the activity bump to drift, thus "searching" the parameter space, possibly to locate a new path to a previously visited goal, without the rat having to physically travel through the space. The mAHP implemented in our model serves the same function as adaptation in Hopfield's model, in that it allows the activity bump to drift forward, in our model also helped by inputs from the conjunctive cells. Thus the "look-ahead" in our model could be described as a "mental time travel" of the attractor map locations just ahead of the rat in Hopfield's terminology. Also, in a regime other than theta during active locomotion, for example sharp waves, the same attractor network with adaptation (resulting from the mAHP or some other intrinsic current) could be used to conduct this mental travel over longer distances and in random directions to plan and encode future routes. Because the code for place is much less sparse in the MEC than in the hippocampus, mental time travel ("look-ahead" or "sweep") occurring simultaneously in many modules of grid cells (each module encoding the environment at a different spatial scale) would find the goal much faster than the same "sweep" across the hippocampal network.

The spatial scale of place and grid fields changes along the dorso-ventral axes of both structures. Individual MEC grid cells, like hippocampal cells, also exhibit changes in spatial scaling under a variety of conditions (Brun et al., 2008; Barry et al., 2007). In our model, spatial scale is determined by two factors: the gain of the self-motion signal (velocity input), and the various after-potential and long-term synaptic currents that result in a "jump-back" of the neural activity bump. It is important to note that many parameters contribute to the distance of the jump-back, and thus influence spatial scale. These include the mAHP and ADP time constants, and the amplitude and time constants of synaptic currents (especially long-term currents). In addition to the changes in time constant of the H-current (Giocomo and Hasselmo, 2008), and the mAHP time constant (Fig. 8), synaptic integrative properties of stellate cells also change along the dorso-ventral axis of the MEC (Garden et al., 2008). Garden et al. (2008) did not look at long-lasting synaptic currents, but they show that the time constant of AMPA currents increase in ventral parts of the MEC. Changes to these parameters have not yet been induced or observed in individual cells *in vivo*, but a decrease in the gain of the self-motion signal is induceable in rats by removing self-motion information derived from motor and proprioception systems, which results in a large expansion of spatial scale in hippocampus (Terrazas et al., 2005). In our model, this gain is the factor used to convert bump movement along the neural ring (in neurons) to position in space (cm). We assume that this factor comes from self motion signals that provide an input to conjunctive cells (possibly via head-direction cells), which is linearly related to the velocity of the animal. At present, little is known about how linear motion signals reach the hippocampal system, although the mammilary nucleus - anterior medial thalamus route is a possibility (Sharp and Turner-Williams, 2005). In the simulations, the relationship between

input to conjunctive cells and movement of the activity bump was linear over a large range of inputs, and as a result, the spatial scale did not vary with the velocity input.

Grid field size (the proportion of a grid period over which a grid cell actually fires), however, may vary independently of the spatial scale (grid spacing). Thus, for example, field size can increase when the rat runs faster, without the grid period (spatial scale) getting larger. If the field size changes, more neurons are active simultaneously, but the population of neurons still encodes the position just as accurately. Thus, this network attractor model predicts that while the spatial scale and period of grid fields stays the same at different running speeds, grid field sizes may increase with running speed, or they may stay the same. Our simulations support both possibilities. In order for field size to stay the same with velocity, the 'jump-back' must stay the same, even though the look-ahead increases with velocity. Thus the ratio of theta frequency to intrinsic burst frequency of the grid cells has to decrease as the rat runs faster. This means the time constants of the currents that cause the re-initiation of spiking should decrease with running speed. These currents could be either the intrinsic currents (ADP and mAHP), which do not change significantly with depolarization (Fig. 8), or the long-lasting excitatory synaptic current, which could also change its time constants or conductance with depolarization. Our simulations showed a slight increase in field sizes with velocity input; however, we could find a linear relationship between the time delay of the ADP and the changes in HD input that maintained field sizes constant with running speed (data not shown). It is plausible that such a relationship could be tuned in the MEC network during postnatal development.

Although it is known that firing rate increases with running speed in most hippocampal formation neurons (e.g., McNaughton et al., 1983), there has been no systematic study of the effect of speed on place field size, in the absence of other possibly confounding variables. From a population vector analysis of the activity of CA1 cells on a within theta cycle time scale, it has been shown that the look-ahead increases as the rat runs faster on a linear track, as our model predicts, but the jump-back may also increase, indicating that the intrinsic oscillation frequency does not compensate adequately, and CA1 field sizes increase (Maurer, 2008); however in these studies running speed is confounded with position on the track and proximity to reward zones.

The prediction that grid field size and spatial period vary independently can be tested in conditions other than varying running speeds. The proportion of spacing over which a grid cell fires can also change, for example as a result of the interactions between the grid cell network and the rest of the hippocampal system. Grid fields are expressed and show phase precession for some time after hippocampal inactivation (Hafting et al., 2008), showing that this network can function alone, but eventually grid cells cease firing, suggesting that hippocampal input is not irrelevant. Such inputs might reset the path integrated grid fields, which are subject to random drift, with information from external landmarks, and may alter path integration by adding different information to the circuit (Burgess et al., 2007). For example, when a rat repeatedly follows the same route, place fields expand opposite to the direction of running (Mehta et al., 1997). This could cause a larger look-ahead in the grid cell network, because of greater input from place cells ahead of the rat during the last part of the theta cycle. If this larger look-ahead does not affect the average progression through grid fields, then grid cells would increase the proportion of the grid period over which they fire in the direction opposite to rat movement, but not the spacing between fields, and the path integrator would still accurately encode distance traveled.

If, however, inputs from place fields are altered due to mismatch between the path integrator and the external landmarks, then rescaling or shifting of grid fields could occur (Samsonovich and McNaughton, 1997). For example, if the active place cells (or other neurons providing a feed back to the grid cell network) cause the bump in the grid cell network to shift and stay ahead, the look-ahead would be larger, but the interburst interval would not change. Thus the average progression through grid fields will be faster, causing a smaller spacing between grid fields. Since the interburst interval and jump-back would not change, grid field sizes would also not change. Barry et al. (2007) conducted a study to cause such a mismatch, in order to determine if grid fields are reset by place cells in response to environmental landmarks. The grid cells in that experiment showed a rescaling of 50% of the resizing of the environment and then a gradual transition to normal scale once the new environment became familiar. These data suggest that the rescaling was not due to a resetting by landmarks (which should cause a 100% rescaling to the environmental boundaries and an abrupt change from landmark-driven to path integration-driven field location), but by a global decrease in the gain of the speed signal in the rescaled dimension. Since the novel environment was smaller than the familiar one, the rat would have seen the walls of the environment approach faster than expected, causing neurons tied to the landmarks to activate sooner than the grid cells driven by path integration. Feedback from landmark-driven cells would cause the look-ahead of the grid cell network to be larger, causing a faster overall movement of the grid cell activity bump through network states, making the spacing between grid fields smaller. The proportion of the spacing in which these cells fire would be larger, because of the larger look-ahead, as appears to be the case in Barry et al. (2007). This value should be measured in future experiments, since the possibility of its variation is a prediction of our model but not of oscillatory interference models.

In conclusion, this model of a network with ring attractor connectivity and intrinsic currents and our simulations of this model, generate three novel predictions which can be tested experimentally. These predictions are different properties of grid cell spikes during late compared to early parts of the theta cycle, the potential for an independent variation of grid field size and spacing, and finally, if field sizes remain constant with running speed, the model predicts a change in time constant of after-spike currents, or amplitude of prolonged excitatory cur-

rents at different running speeds. The first two predictions could be measured in multiple phenomena already studied with electrophysiological recordings from the MEC of behaving rats. The conjecture that grid cell spikes have different properties during late compared to early parts of the theta cycle suggests, for example, that there is a different slope of phase precession at entry into a grid field compared to the exit out of a field, and that grid fields are asymmetrical in different running directions. Independent variation in grid spatial period and field size could be observed, for example, at different running speeds of the animal, or during experience-dependent changes in field sizes.

METHODS

Simulations

An attractor map model of grid and conjunctive cells was created, with connectivity according to the toroidal attractor map theory (Samsonovich and McNaughton, 1997; McNaughton et al., 2006). For simplicity, the model was implemented in 1D, making it equivalent in terms of connectivity to the Skaggs et al. (1995) ring attractor model for head direction cells (see also Zhang, 1996).

Grid and conjunctive cells were implemented as leaky integrate and fire neurons, connected by synapses. The membrane voltage (V) of each neuron dynamically changes as follows:

$$\tau_m \frac{dV}{dt} = E_L - V - \sum_j w_{ij} p_j (V - E_s) + R_m I_{ext}$$

where $\tau_m = 10$ ms is the membrane time constant, $E_L = -70$ mV is the leak reversal potential, and E_S is the synaptic reversal potential, set at 0 mV for excitatory synapses, and -80 mV for inhibitory synapses. Inputs from sources external to the grid and conjunctive cell network, including initial input to grid cells to cause an activity bump to form, and input about head-direction to the conjunctive cells (see below for full explanation of head direction inputs) are modeled as external currents ($R_m I_{ext}$). Grid cells also had an intrinsic conductance, modeled to mimic the after-spike potentials of stellate cells, to generate intrinsic oscillatory activity, which contributes to theta phase precession (see below). When the membrane voltage reached threshold (-54 mV), a spike was recorded, and V was reset to -80 mV. Simulations were run in MATLAB, using the Euler method of integration.

AMPA synapses were modeled as conductance changes following a presynaptic spike, with the proportion of open channels decaying as a single exponential. Two ms after a spike occurred in a presynaptic neuron (j), the proportion open channels in that synapse (p_j) was set to 1, and then exponentially decayed with a time constant of 10 ms. The weight of each synapse (w_{ij}) determined its maximal conductance. Excitatory synapses were probabilistic. The probability of transmission of each presynaptic spike was 0.5.

The synaptic connectivity was implemented as a ring attractor network. Grid cells can be schematically arranged according to the relative phase offsets of their grid fields. Because phase is periodic, the network boundaries are also periodic (i.e., a ring). Each neuron was connected to others with synaptic strength decreasing as a Gaussian function of distance (see Figs. 1A,B). Interneurons were not explicitly modeled, but inhibitory feedforward and feedback connections, with a delay of 4 ms and a 10 ms decay time, were added between all groups of excitatory neurons, to regulate the total activity of all grid cells and conjunctive cells. Thus, activity stayed in a "bump" corresponding to one location (see Fig. 3A). There were two groups of conjunctive cells, each corresponding to opposite head directions ("north" and "south"), each of which contained the same number of neurons as there were grid cells. Each grid cell had a synaptic connection to its corresponding conjunctive cell in each group, as well as their near neighbors, with synaptic strength again falling off with distance in a Gaussian manner (See Table I for parameters). Each conjunctive cell had synapses onto the grid cells corresponding to a position offset (11 neurons counterclockwise for the "north" conjunctive cells) from that represented by the conjunctive cell. Again, there was a Gaussian spread of synaptic connections to a group of grid cells. Inhibitory synapses were present on all conjunctive cells and activated based on the activity of the conjunctive cells of both groups, in order to allow only a small group of conjunctive cells of one head direction to be active at a time (Fig. 1C). Therefore, when a "north" head direction input activated one group of conjunctive cells, the conjunctive cells corresponding to the location of the activity bump in the grid cell network spiked, and moved the bump in the counterclockwise direction (see Fig. 3A). The synaptic connectivity pattern modeled here was designed based on previous attractor models of path integration (Samsonovich and McNaughton, 1997), with less attention paid to evidence of actual connectivity patterns in the superficial layers of the MEC, because this evidence is very limited. Other connectivity patterns that could create an attractor network are plausible, however.

In addition to AMPA and $GABA_A$—like synapses, NMDA synapses between grid cells were simulated. A long time constant current such as this was necessary in order to allow grid cells to be activated over multiple theta cycles. NMDA-like synaptic events were activated every time an AMPA synaptic event at the same grid cell-grid cell synapse occurred, thus also with a probability of 0.5 and 2 μs following a presynaptic spike. The time course of NMDA channel opening was modeled as a difference of exponentials (Destexhe et al., 1994; reviewed in Dayan and Abbot, 2001, pp. 180–183), with a rise time of 2 ms and a fall time of 150 μs (or somewhere between 125 and 500 ms in Fig. 5). The maximal conductance (weight) of these synapses was based on the weight of the AMPA synapses between the same neurons, with a fixed NMDA:AMPA weight ratio for all grid cell to grid cell synapses. (The NMDA weight was 2^*w_{ij} in simulations in which the NMDA fall time constant was 150 ms. The NMDA:AMPA ratio was changed with NMDA fall time to keep the firing rates the same for all

simulations in Fig. 5). The conductance of NMDA synapses also depended on the neurons' voltage, based on the relationship determined by Jahr and Stevens (1990; reviewed in Dayan and Abbot, 2001, p. 183):

$$G_{\mathrm{NMDA}} = \left[1 + \frac{[\mathrm{Mg}^{2+}]}{3.57\mathrm{mM}} * e^{-\mathrm{V}/16.13\mathrm{mV}}\right]^{-1}$$

A magnesium concentration of 0.1 mM was assumed, giving the voltage dependency of excitatory synaptic connections shown in Figure 1C.

Inputs to the model included a source of theta modulation, and a velocity modulated head-direction input, both presented to the conjunctive cells. All conjunctive cells received an 8-Hz sine wave current input, 8 mV in amplitude, throughout the simulation, causing the activity of the conjunctive cells to be "theta" modulated. Head direction input was added to the model as a constant current input into one group of conjunctive cells (usually the "north" conjunctive cells). The amplitude of this input was varied from 1 to 8 mV, to simulate different running speeds. Head direction cells in the MEC have been shown to be velocity modulated (Sargolini et al., 2006).

The medium after-hyperpolarization (mAHP), and after-depolarization (ADP) phenomena of stellate cells were modeled in the simulated grid cells as conductance changes following each spike. Since the mAHP is likely caused by the closing of H-channels (Fransen et al., 2004), a conductance with a reversal potential of -20 mV was added to the grid cells. The leak reversal potential was changed to -80 mV, and the H-conductance was set so that before a spike, the resting potential of the cell remained at -70 mV. Following each spike, the proportion of open H-channels first decreased, to cause the mAHP, and then increased, to cause the ADP, according to summation of the equations:

$$p_{\mathrm{mAHP}} = 0.5 - 0.5 * e^{-t/a}$$

$$p_{\mathrm{ADP}} = 0.5 * e^{-(t-b)^2/(2*c^2)}$$

where t is the time following the last spike, and a, b, and c are time constants representing the decay of the mAHP, delay of the ADP peak, and width of the ADP peak, respectively. These time constants were set to mimic the stellate cell after-spike potential data, and varied proportionally (from $a = 40$, $b = 80$, $c = 24$ to $a = 115$, $b = 230$, $c = 69$) to represent changes in the H-current time constants along the dorso-ventral axis of the MEC, resulting in the after-spike membrane potential profiles shown in Figure 4A. Note that the mAHP and ADP were not modeled in the conjunctive cells, based on physiological data showing the absence of H-current dynamics and ADP in MEC Layer III neurons (Dickson et al., 1997).

The movement of the grid network "activity bump" during a run of the simulation was analyzed by calculating the position (neuron) of the center of mass of the activity of all of the grid cells in every 10-ms bin. This position was then used to linearize the movement of the bump along the circular arrangement of grid cells, to determine cumulative movement. The movement within a theta cycle was analyzed by aligning the average positions over every two theta cycles, and averaging the activity in each of those two-theta-cycle periods over the entire simulation. Grid fields were analyzed by finding the first and last spike during each pass through the field for each neuron. Grid fields that began >100 ms after the formation of the activity bump, and end <150 ms before the end of the simulation were used. The time between the first and last spike of each field was used as a measure of grid field size. The center of mass of the spikes within each field was then found, and the peak of theta nearest to that center of mass was used to align all fields to one another. This produced the Skaggs plot of theta phase precession (Skaggs et al., 1996; Fig. 3C). The spike time relative to the center of mass of the field the spike belonged to was plotted vs. the theta phase of that spike to create the theta phase vs. position plots (Fig. 3E).

The average autocorrelation of all grid cells was used to determine the intrinsic oscillation of the grid cells and grid field spacing in each simulation. Two oscillations were evident in the autocorrelation: an interburst frequency of ~120 ms, within a slower beat frequency that indicated the spacing of the grid fields. The autocorrelation was convolved with a hanning window of 25 ms, to extract the intrinsic oscillation peaks. Grid field spacing was determined by convolving with a hanning window of the grid field size.

Slice Physiology

Methods for slice physiology and stellate cell *in vitro* whole-cell patch clamp recordings have been described previously (Giocomo et al., 2007). A total of 46 stellate cells were analyzed. Of the 46 cells, 25 came from the dorsal portion of MEC (3.8–4.9 mm from the dorsal surface of the brain) and 19 came from the ventral portion of MEC (5.0–6.0 mm from the dorsal surface of the brain).

All experimental data were analyzed in MATLAB. To determine the time constant of the medium AHP and characteristic of ADP the portion of the AHP just after a single action potential was fit with the following dual exponential equation:

$$V(t) = V(0) - z\left(\frac{\tau_{\mathrm{R}}\tau_{\mathrm{O}}}{\tau_{\mathrm{R}} - \tau_{\mathrm{O}}}\right)\left(e^{-t/\tau_{\mathrm{R}}} - e^{-t/\tau_{\mathrm{O}}}\right)$$

where $V(t)$ is the membrane potential as a function of time (t). $V(0)$ is the baseline membrane potential (corresponding to the initial value and eventual highest positive value reached after the mAHP). z is a constant used as a scaling factor proportional to the magnitude of the mAHP. τ_{O} is the measured onset time constant (rate of hyperpolarization), and τ_{R} is the time constant of recovery (depolarization) back to the initial membrane potential value. To determine the half width, the trough value and eventual highest positive value reached after the mAHP (as determined by the time constant fit) were used to determine the time point (half max) where the width of the AHP was measured. For time constant data, analysis was used from cells which had >5 action potentials with good fits, as determined by an average adjusted R^2 of > 0.85. The average

number of spikes analyzed was 22 ± 2. Spikes were analyzed that came from portions of the data where the cell was near its firing threshold (−55 to −40 mV). Data analysis was conducted using MATLAB (Mathworks) and Excel (Microsoft). To test the difference between samples (e.g., dorsal vs. ventral) the nonparametic Kolmogorov-Smirnov (ks) test was used. Correlations were tested using the Spearman's rank correlation coefficient. For all analysis, a value of $P < 0.05$ was considered significant. Regression lines were constructed using the least squares method in Microsoft Excel and the R values are reported.

REFERENCES

Amari S. 1977. Dynamics of pattern formation in lateral-inhibition type neural fields. Biol Cybern 27:77–87.

Barry C, Hayman R, Burgess N, Jeffery KJ. 2007. Experience-dependent rescaling of entorhinal grids. Nat Neurosci 10:682–684.

Ben-Yishai R, Bar-Or RL, Sompolinsky H. 1995. Theory of orientation tuning in visual cortex. Proc Natl Acad Sci USA 92:3844–3848.

Blair HT, Welday AC, Zhang K. 2007. Scale-invariant memory representations emerge from moiré interference between grid fields that produce theta oscillations: A computational model. J Neurosci 27:3211–3229.

Brun VH, Solstad T, Kjelstrup KB, Fyhn M, Witter MP, Moser EI, Moser MB. 2008. Progressive increase in grid scale from dorsal to ventral medial entorhinal cortex. Hippocampus 18:1200–1212.

Burgess N, Recce M, O'Keefe J. 1994. A model of hippocampal function. Neural Networks 7:1065–1081.

Burgess N, Barry C, O'Keefe J. 2007. An oscillatory interference model of grid cell firing. Hippocampus 17:801–812.

Burgess N. 2008. Grid cells and theta as oscillatory interference: Theory and predictions. Hippocampus 18:1157–1174.

Buszaki G. 2006. Rhythms of the Brain. New York: Oxford University Press, Inc.448p.

Chen LL, Lin L-H, Green EJ, Barnes CA, McNaughton BL. 1994. Head-direction cells in the rat posterior cortex. I. Anatomical distribution and behavioral modulation. Exp Brain Res 101:8–23.

Compte A, Brunel N, Goldman-Rakic PS, Wang X-J. 2000. Synaptic mechanisms and network dynamics underlying spatial working memory in a cortical network model. Cereb Cortex 10:910–923.

Conklin J, Eliasmith C. 2005. An attractor network model of path integration in the rat. J Comp Neurosci 18:183–203.

Dayan P, Abbot LF. 2001. Theoretical Neuroscience. Cambridge, MA: The MIT Press.460p.

Destexhe A, Mainen ZF, Sejnowski TJ. 1994. Synthesis of models for excitable membranes, synaptic transmission and neuromodulation using a common kinetic formalism. J Comput Neurosci 1:195–230.

Dhillon A, Jones RS. 2000. Laminar differences in recurrent excitatory transmission in the rat entorhinal cortex in vitro. Neuroscience 99:413–422.

Dickson CT, Mena AR, Alonso A. 1997. Electroresponsiveness of medial entorhinal cortex layer III neurons in vitro. Neuroscience 81:937–950.

Dickson CT, Magistretti J, Shalinsky MH, Fransen E, Hasselmo ME, Alonso A. 2000. Properties and role of I(h) in the pacing of subthreshold oscillations in entorhinal cortex layer II neurons. J Neurophysiol 83:2562–2579.

Doboli S, Minai AA, Best PJ. 2000. Latent attractors: A model for context-dependent place representations in the hippocampus. Neural Comp 12:1009–1043.

Fernandez FR, White JA. 2008. Artificial synaptic conductances reduce subthreshold oscillations and periodic firing in stellate cells of the entorhinal cortex. J Neurosci 28:3790–3803.

Fiete I, Burak Y, Brookings T. 2008. What grid cells convey about rat location. J. Neurosci 28:6858–6871.

Fransén E, Alonso AA, Dickson CT, Magistretti J, Hasselmo ME. 2004. Ionic mechanisms in the generation of subthreshold oscillations and action potential clustering in entorhinal layer II stellate neurons. Hippocampus 14:368–384.

Fuhs MC, Touretzky DS. 2006. A spin glass model of path integration in rat medial entorhinal cortex. J Neurosci 26:4266–4276.

Fyhn M, Molden S, Witter MP, Moser EI, Moser MB. 2004. Spatial representation in the entorhinal cortex. Science 305:1258–1264.

Fyhn M, Hafting T, Treves A, Moser MB, Moser EI. 2007. Hippocampal remapping and grid realignment in entorhinal cortex. Nature 446:190–194.

Garden DL, Dodson PD, O'Donnell C, White MD, Nolan MF. 2008. Tuning of synaptic integration in the medial entorhinal cortex to the organization of grid cell firing fields. Neuron 60:875–889.

Germroth P, Schwerdtfeger WK, Buhl EH. 1989. Morphology of identified entorhinal neurons projecting to the hippocampus. A light microscopical study combining retrograde tracing and intracellular injection. Neuroscience 30:683–691.

Giocomo LM, Zilli EA, Fransen E, Hasselmo ME. 2007. Temporal frequency of subthreshold oscillations scales with entorhinal grid cells field spacing. Science 315:1719–1722.

Giocomo LM, Hasselmo ME. 2008. Time constants of h current in layer II stellate cells differ along the dorsal to ventral axis of medial entorhinal cortex. J Neurosci 28:9414–9425.

Guanella A, Kiper D, Verschure P. 2007. A model of grid cells based on a twisted torus topology. Int J Neural Syst 17:231–240.

Hafting T, Fyhn M, Molden S, Moser MB, Moser EI. 2005. Microstructure of a spatial map in the entorhinal cortex. Nature 436:801–806.

Hafting T, Fyhn M, Bonnevie T, Moser MB, Moser EI. 2008. Hippocampus-independent phase precession in entorhinal grid cells. Nature 453:1248–1252.

Harvey CD, Collman F, Dombeck DA, Tank DW. 2009. Intracellular dynamics of hippocampal place cells during virtual navigation. Nature 461:941–946.

Hasselmo ME, Brandon MP. 2008. Linking cellular mechanisms to behavior: entorhinal persistent spiking and membrane potential oscillations may underlie path integration, grid cell firing, and episodic memory. Neural Plast 2008:658323.

Hebb DO. 1949. The Organization of Behavior. New York: Wiley.

Hopfield JJ. 2010. Neurodynamics of mental exploration. Proc Natl Acad Sci 107:1648–1653.

Jahr CE, Stevens CF. 1990. A quantitative description of NMDA receptor-channel kinetic behavior. J Neurosci 10:1830–1837.

Jensen O, Lisman JE. 1996. Hippocampal CA3 region predicts memory sequences: Accounting for the phase precession of place cells. Learn Mem 3:279–287.

Jung MW, Wiener SI, McNaughton BL. 1994. Comparison of spatial firing characteristics of units in dorsal and ventral hippocampus of the rat. J Neurosci 14:7347–7356.

Klink R, Alonso A. 1993. Ionic mechanisms for the subthreshold oscillations and differential electroresponsiveness of medial entorhinal cortex layer II neurons. J Neurophysiol 70:144–157.

Kropff E, Treves A. 2008. The emergence of grid cells: Intelligent design or just adaptation? Hippocampus 18:1256–1269.

Kumar SS, Jin X, Buckmaster PS, Huguenard JR. 2007. Recurrent circuits in layer II of medial entorhinal cortex in a model of temporal lobe epilepsy. J Neurosci 27:1239–1246.

Lingenhohl K, Finch DM. 1991. Morphological characterization of rat entorhinal neurons *in vivo*: Soma-dendritic structure and axonal domains. Exp Brain Res 84:57–74.

Lisman JE, Idiart MA. 1995. Storage of 7 +/- 2 short-term memories in oscillatory subcycles. Science 267:1512–1515.
Lisman J, Redish AD. 2009. Prediction, sequences and the hippocampus. Philos Trans R Soc Lond B Biol Sci 364:1193–1201.
Maurer AP, Vanrhoads SR, Sutherland GR, Lipa P, McNaughton BL. 2005. Self-motion and the origin of differential spatial scaling along the septo-temporal axis of the hippocampus. Hippocampus 15:841–852.
Maurer AP, McNaughton BL. 2007. Network and intrinsic cellular mechanisms underlying theta phase precession of hippocampal neurons. Trends Neurosci 30:325–333.
Maurer AP. 2008.PhD Dissertation, Neuroscience Program, University of Arizona: Tucson AZ.
McNaughton BL, Barnes CA, O'Keefe J. 1983. The contributions of position, direction, and velocity to single unit activity in the hippocampus of freely-moving rats. Exp Brain Res 52:41–49.
McNaughton BL, Barnes CA, Gerrard JL, Gothard K, Jung MW, Knierim JJ, Kudrimoti H, Qin Y, Skaggs WE, Suster M, Weaver KL. 1996. Deciphering the hippocampal polyglot: The hippocampus as a path integration system. J Exp Biol 199:173–185.
McNaughton BL, Battaglia FP, Jensen O, Moser EI, Moser MB. 2006. Path integration and the neural basis of the 'cognitive map'. Nat Rev Neurosci 7:663–678.
Mehta MR, Barnes CA, McNaughton BL. 1997. Experience-dependent, asymmetric expansion of hippocampal place fields. Proc Natl Acad Sci USA 94:8918–8921.
Mizumori SJ, Williams JD. 1993. Directionally selective mnemonic properties of neurons in the lateral dorsal nucleus of the thalamus of rats. J Neurosci 13:4015–4028.
O'Keefe J, Dostrovsky J. 1971. The hippocampus as a spatial map. Preliminary evidence from unit activity in the freely-moving rat. Brain Res 34:171–175.
O'Keefe J. 1976. Place units in the hippocampus of the freely moving rat. Exp Neurol 51:8–109.
O'Keefe J, Nadel L. 1978. The Hippocampus as a Cognitive Map. Oxford; Oxford University Press.
O'Keefe J, Recce ML. 1993. Phase relationship between hippocampal place units and the EEG theta rhythm. Hippocampus 3:317–330.
O'Keefe J, Burgess N. 2005. Dual phase and rate coding in hippocampal place cells: Theoretical significance and relationship to entorhinal grid cells. Hippocampus 15:853–866.
Redish AD, McNaughton BL, Barnes CA. 2000. Place cell firing shows an inertia-like process. Neurocomputing 32-33:235–241.
Remme MW, Lengyel M, Gutkin BS. 2009. The role of ongoing dendritic oscillations in single-neuron dynamics. PLoS Comput Biol 5:e1000493.
Samsonovich A, McNaughton BL. 1997. Path integration and cognitive mapping in a continuous attractor neural network model. J Neurosci 17:5900–5920.
Sargolini F, Fyhn M, Hafting T, McNaughton BL, Witter MP, Moser MB, Moser EI. 2006. Conjunctive representation of position, direction, and velocity in entorhinal cortex. Science 312:758–762.
Sharp PE, Turner-Williams S. 2005. Movement-related correlates of single-cell activity in the medial mammillary nucleus of the rat during a pellet chasing task. J Neurophysiol 94:1920–1927.
Skaggs WE, Knierim JJ, Kudrimoti HS, McNaughton BL. 1995. A model of the neural basis of the rat's sense of direction. In: Tesauro G, Touretzky D, Leen T, editors. Advances in Neural Information Processing Systems. Cambridge, MA: MIT Press. pp130–180.
Skaggs WE, McNaughton BL, Wilson MA, Barnes CA. 1996. Theta phase precession in hippocampal neuronal populations and the compression of temporal sequences. Hippocampus 6:149–172.
Solstad T, Moser EI, Einevoll GT. 2006. From grid cells to place cells: a mathematical model. Hippocampus 16:1026–1031.
Taube JS, Muller RU, Ranck JB. 1990. Head direction cells recorded from the postsubiculum in freely moving rats. I. Description and quantitative analysis. J Neurosci 10:420–435.
Taube JS. 1995. Head direction cells recorded in the interior thalamic nuclei of freely moving rats. J Neurosci 15:70–86.
Terrazas A, Krause M, Lipa P, Gothard KM, Barnes CA, McNaughton BL. 2005. Self-motion and the hippocampal spatial metric. J Neurosci 25:8085–8096.
Tsodyks MV, Skaggs WE, Sejnowski TJ, McNaughton BL. 1996. Population dynamics and theta rhythm phase precession of hippocampal place cell firing: A spiking neuron model. Hippocampus 6:271–280.
Wallenstein GV, Hasselmo ME. 1997. GABAergic modulation of hippocampal population activity: Sequence learning, place field development, and the phase precession effect. J Neurophysiol, 78:393–408.
West PJ, Dalpé-Charron A, Wilcox KS. 2007. Differential contribution of kainate receptors to excitatory postsynaptic currents in superficial layer neurons of the rat medial entorhinal cortex. Neuroscience 146:1000–1012.
Witter MP, Moser EI. 2006. Spatial representation and the architecture of the entorhinal cortex. Trends Neurosci 29:671–678.
Zhang K. 1996. Representation of spatial orientation by the intrinsic dynamics of the head direction cell ensemble: A theory. J Neurosci 16:2112–2126.
Zilli EA, Yoshida M, Tahvildari B, Giocomo LM, Hasselmo ME. 2009. Evaluation of the oscillatory interference model of grid cell firing through analysis and measured period variance of some biological oscillators. PLoS Comput Biol 5:e1000573.